



# Aeroacoustic time-reversal in the presence of a reflecting surface

Akhilesh Mimani<sup>1</sup>; Con J. Doolan<sup>2</sup>; Paul R. Medwell<sup>3</sup>

<sup>1,2,3</sup>School of Mechanical Engineering, The University of Adelaide, South Australia – 5005, Australia

## ABSTRACT

The influence of a rigid-wall reflecting surface on aeroacoustic Time-Reversal (TR) is investigated in this work. To this end, a forward simulation of a Gaussian pulse propagation in 2-D computational domain with a uniform mean flow was implemented by numerically solving the Linearised Euler Equations subject to a rigid-wall condition (by setting the normal velocity to zero) at the bottom boundary modelling the reflecting condition. The anechoic conditions were implemented at the remaining three boundaries, thereby modelling a semi-infinite 2-D free-space. The acoustic pressure time-history was stored at all boundaries during the forward simulation. A set of TR simulations were carried out wherein rigid-wall condition was implemented at bottom boundary in each of the test-cases and time-reversed acoustic pressure was enforced at (1) all four boundaries, (2) three boundaries excluding the bottom boundary, (3) the top and bottom boundaries and (4) only the top boundary in the first, second, third and fourth test-case, respectively. It was observed that the initial emission point of the pulse was accurately predicted in all four test-cases, thereby demonstrating that acoustic pressure need not be measured at the rigid-wall. Rather, taking advantage of wave-reflection, only one microphone Line Array located outside flow can be used during aeroacoustic TR for source localisation.

Keywords: Source localization and transmission paths (74.6), Processing by microphone arrays (74.7) and Reflection and echoes (23.2)

## 1. INTRODUCTION

The acoustic Time-Reversal (TR) proposed by Fink *et al.* (1, 2) is a robust method operating in the time-domain used for solving inverse problems of sound source localisation. Enforcing the time-reversed acoustic pressure (recorded at microphone Line Arrays (LAs) during experiments or stored on nodes (virtual microphones) at the computational boundaries at every time-step during forward simulation) boundary conditions during TR simulation enables the back-propagation of waves into the domain towards the source location (3). A limited angular aperture LA in a Time-Reversal Mirror (TRM) that only partially encloses a source, intercepts and records only a fraction of the radiated acoustic pressure field (1, 2), thereby limiting the ability of TR to accurately predict the location and the source nature. However, a LA configuration in a TRM completely enclosing the source intercepts the wave propagating in all directions. Therefore, the back-propagation of waves from such a LA configuration during TR yields the most accurate prediction of the location and characteristics of the aeroacoustic source (4, 5), whilst the shape and strength of a transient signal (a Gaussian pulse) can also be recovered exactly (6). However, setting up of such a LA configuration may be difficult in an aeroacoustics experiment, such as in a wind tunnel due to the number of microphones required (increasing with the source frequency due to Nyquist-Shannon spatial-sampling criteria (1, 7)) and also because the microphones must be located outside the flow field (3, 4).

Padois *et al.* (3) used acoustic pressure time-history measured over one LA of microphones (located outside the flow) to localise time-harmonic monopole source (modelled by a loudspeaker) and dipole sources (simulated by two loudspeakers in proximity with their axis parallel to flow) in a wind tunnel flow using TR simulation. The main limitation in their work is the use of only one LA which cannot record sufficient acoustic pressure time-history data required during TR simulation for resolving practically

---

<sup>1</sup>[akhilesh.mimani@adelaide.edu.au](mailto:akhilesh.mimani@adelaide.edu.au)

<sup>2</sup>[con.doolan@adelaide.edu.au](mailto:con.doolan@adelaide.edu.au)

<sup>3</sup>[paul.medwell@adelaide.edu.au](mailto:paul.medwell@adelaide.edu.au)

important flow-induced noise sources such as a lift dipole (axis perpendicular to flow) generated by a cross-flow over cylinder, air-foil or a flat-plate (8). The present authors previously demonstrated using aeroacoustic TR simulations (based on *simulated* experimental data) that a minimum of two LAs located at the top and bottom boundaries of an Anechoic Wind Tunnel (AWT) outside the flow field is necessary and indeed, sufficient to characterise time-harmonic idealised monopole and dipole (axis perpendicular to flow) sources (5). This is because at a *non-reflective* (anechoic) boundary, it is important to intercept the acoustic wave fronts and record the acoustic pressure time-history using microphone LAs to obtain the corresponding boundary data. However, at a perfectly reflecting surface such as a rigid floor in the wind tunnel, the incident acoustic wave fronts are reflected and a significant fraction of the reflected wave fronts can propagate towards and be intercepted by the microphone LA located near the anechoic boundary. Therefore, from a theoretical point-of-view, the use of only a single LA of microphones in the presence of a rigid surface at the opposite boundary can record sufficient boundary data for characterising flow-induced dipole noise sources. Indeed, previous studies (in a stationary medium) have indicated that TR method can take into account a reflecting surface (9), is robust in a reverberating environment (10, 11), in fact, TR source resolution is enhanced in the presence of multiple scatters (12) in the near-field of the source.

In light of the foregoing discussion, this paper investigates for the first time, the influence of a perfectly reflecting surface (modelled by a rigid wall) on the accuracy of aeroacoustic TR source localisation through a benchmark problem of propagation of a Gaussian pulse in a uniform mean flow (13). The objective of this work is then to demonstrate the potential advantage offered by wave reflection at a rigid surface; the acoustic pressure time-history need not be recorded at a rigid surface without compromising on the accuracy of source localisation, thereby reducing the number of microphones required.

## 2. METHODOLOGY: DETAILS OF THE NUMERICAL IMPLEMENTATION

An algorithm for the numerical implementation of the forward and TR simulations of acoustic wave propagation on a 2-D semi-infinite free-space is briefly described. To this end, a schematic of the 2-D computational domain given by  $x \leq |L_x + \Delta L_x|$ ,  $-L_y \leq y \leq L_y + \Delta L_y$  with a rigid wall at the bottom boundary  $y = -L_y$ , and a sponge-layer domain surrounding the computational domain on the remaining three boundaries is considered in Fig. 1. The sponge-layer domain damps the incoming acoustic waves, thereby minimising the reflections from the exterior computational boundaries (6) whilst the reflective condition at the bottom boundary is implemented by a rigid wall, thereby modelling a 2-D semi-infinite free-space.

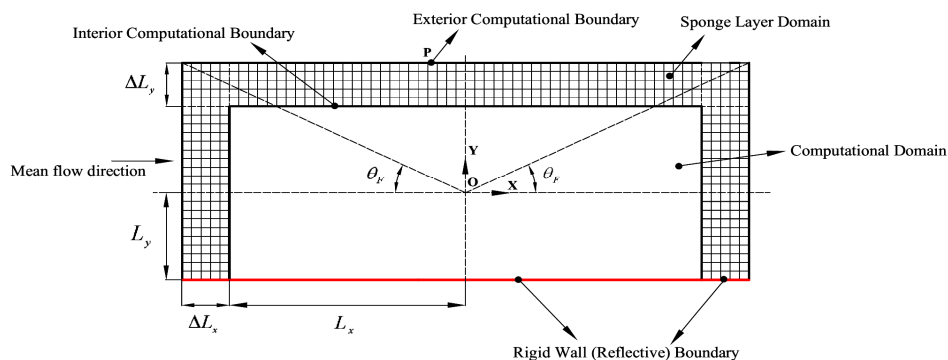


Figure 1 – A rectangular domain with a rigid wall at the bottom boundary modelling a 2-D semi-infinite free-space.

The half-lengths of the computational domain along the  $x$  and  $y$  directions are given by  $L_x = 1.5$  m and  $L_y = 0.5$  m, respectively, (ensuring a high aspect-ratio  $L_x/L_y = 3$  during the TR) whilst width of the sponge-layer is taken as  $\Delta L_x = \Delta L_y = 0.15$  m. The number of nodes along the  $x$  and  $y$  directions in the computational domain are given by  $N_x = (2L_x/\Delta x) + 1 = 601$  and  $N_y = (2L_y/\Delta y) + 1 = 201$ , respectively,

whilst that in sponge-layer domain is given by  $N_{\text{sponge}} = \Delta L_x / \Delta x = \Delta L_y / \Delta y = 30$ , respectively, where equal mesh size  $\Delta x = \Delta y = \Delta n = 0.005$  m is considered to ensure accurate wave propagation over a large frequency range. As indicated in Fig. 1, the direction of the subsonic uniform mean flow is considered towards the positive  $x$  direction during the forward simulation.

## 2.1 Forward Simulation

The forward simulation of a Gaussian pulse in the 2-D semi-finite space (shown in Fig. 1) is implemented by numerically solving the homogenous 2-D Linearised Euler Equations (LEE), assuming homoentropic flow conditions given by (14)

$$\frac{\partial \tilde{p}}{\partial t} + U_0 \frac{\partial \tilde{p}}{\partial x} + \rho_0 \left( \frac{\partial \tilde{u}}{\partial x} + \frac{\partial \tilde{v}}{\partial y} \right) = 0, \quad \rho_0 \frac{\partial \tilde{u}}{\partial t} + \rho_0 U_0 \frac{\partial \tilde{u}}{\partial x} + \frac{\partial \tilde{p}}{\partial x} = 0, \quad \rho_0 \frac{\partial \tilde{v}}{\partial t} + \rho_0 U_0 \frac{\partial \tilde{v}}{\partial x} + \frac{\partial \tilde{p}}{\partial y} = 0, \quad (1a-c)$$

where  $\tilde{p}(x, y, t)$ ,  $\tilde{\rho}(x, y, t)$ ,  $\tilde{u}(x, y, t)$  and  $\tilde{v}(x, y, t)$  are the acoustic pressure (Pa), acoustic density ( $\text{kg} \cdot \text{m}^{-3}$ ) and acoustic particle velocities ( $\text{m} \cdot \text{s}^{-1}$ ) along the  $x$  and  $y$  direction, respectively,  $\rho_0$  is the ambient density, taken as  $1.21 \text{ kg} \cdot \text{m}^{-3}$ ,  $t$  is the forward time (s). In Eqs. (1a-c),  $U_0$  is the subsonic uniform mean flow velocity towards positive  $x$  direction. The forward simulations are implemented by first substituting the isentropic conditions in Eqs. (1a-c) and recasting the resultant equations into the Pseudo-Characteristic Formulation, henceforth denoted by PCF (15)

$$\begin{aligned} \frac{\partial \tilde{p}}{\partial t} &= -\frac{\rho_0 c_0}{2} \left\{ (X_{\text{linear}}^+ + X_{\text{linear}}^-) + (Y_{\text{linear}}^+ + Y_{\text{linear}}^-) \right\}, \\ \frac{\partial \tilde{u}}{\partial t} &= -\frac{1}{2} (X_{\text{linear}}^+ - X_{\text{linear}}^-), \quad \frac{\partial \tilde{v}}{\partial t} = -\frac{1}{2} (Y_{\text{linear}}^+ - Y_{\text{linear}}^-) - c_0 M_0 \frac{\partial \tilde{v}}{\partial x}, \end{aligned} \quad (2a-c)$$

$$\text{where} \quad X_{\text{linear}}^\pm = \pm c_0 (1 \pm M_0) \left\{ \frac{1}{\rho_0 c_0} \frac{\partial \tilde{p}}{\partial x} \pm \frac{\partial \tilde{u}}{\partial x} \right\} \quad \text{and} \quad Y_{\text{linear}}^\pm = \pm c_0 \left\{ \frac{1}{\rho_0 c_0} \frac{\partial \tilde{p}}{\partial y} \pm \frac{\partial \tilde{v}}{\partial y} \right\}. \quad (3, 4)$$

In Eqs. (2a-c),  $X_{\text{linear}}^+$  denotes the acoustic flux propagating towards the positive  $x$  direction with an enhanced speed of  $c_0(1+M_0)$ , whilst  $X_{\text{linear}}^-$  denotes the acoustic flux propagating towards the negative  $x$  direction with a reduced speed of  $c_0(1-M_0)$ , respectively. Similarly,  $Y_{\text{linear}}^\pm$  denotes fluxes propagating with sound speed  $c_0$  towards the positive and negative  $y$  directions, respectively. Furthermore,  $M_0 = U_0/c_0$  is the Mach number taken equal to 0.3 in this work.

### 2.1.1 Computation of the spatial-derivatives and time-integration

The spatial derivatives in fluxes propagating along the positive  $(X_{\text{linear}}^+, Y_{\text{linear}}^+)$  and negative  $(X_{\text{linear}}^-, Y_{\text{linear}}^-)$  directions are computed using overall upwind-biased FD schemes implemented as matrix-column multiplication shown as (16, 17)

$$\frac{\partial \{\psi\}^+}{\partial n} \approx \frac{1}{\Delta n} [\mathbf{R}_1] \{\psi\} \quad \text{and} \quad \frac{\partial \{\psi\}^-}{\partial n} \approx \frac{1}{\Delta n} [\mathbf{R}_2] \{\psi\}, \quad (5, 6)$$

respectively, where  $\{\psi\} = \{\psi_1, \psi_2, \psi_3, \dots, \psi_N\}^T$  represents either the acoustic pressure or the acoustic particle velocities. Here,  $[\mathbf{R}_1]$  and  $[\mathbf{R}_2]$  are the overall upwind-biased FD scheme matrices formulated using (a) 4<sup>th</sup> order, 7-point optimised upwind biased FD scheme of Zhuang and Chen (18) at interior nodes,

(b) the 5<sup>th</sup> and 3<sup>rd</sup> order standard upwind-biased FD schemes (19) near the boundary nodes, (c) the 7-point optimised one-sided FD scheme by Zhuang and Chen (18) at the penultimate nodes and (d) the 7-point optimised backward FD scheme of Tam (20) at the boundary nodes. It is noted that  $\{\psi\}$  represents either the acoustic pressure or particle velocities,  $N$  stands for  $N_x$  or  $N_y$  and  $\Delta n$  represents  $\Delta x$  or  $\Delta y$ . It is noted that since the mean flow is assumed to be towards the positive  $x$  direction, the spatial derivative  $c_0 M_0 (\partial \tilde{v} / \partial x)$  in Eq. (2) is computed using Eq. (5). The 3<sup>rd</sup> order Total-Variation-Diminishing Runge-Kutta scheme (21) is used for time-integration during the forward and TR simulations. The time-step  $\Delta t$  considered is computed in accordance with the following Courant–Friedrichs–Lewy (CFL) condition (21).

$$CFL = \frac{(1 + M_0) c_0 \Delta t}{\Delta x} \leq 1. \quad (7)$$

In this work,  $CFL = 0.2$  is considered to ensure accuracy of the forward and the TR simulations. Based on the geometrical and simulation parameters chosen,  $\Delta t = 2.24175 \times 10^{-6}$  s.

### 2.1.2 Implementation of the anechoic and rigid (reflecting) boundary conditions

The first-order Clayton-Engquist-Majda (CEM) boundary conditions (22) were implemented at nodes on the  $x = \pm (L_x + \Delta L_x)$  and  $y = L_y + \Delta L_y$  boundaries to model the anechoic boundary conditions (ABCs) whilst the special corner boundary conditions (23) were implemented at the two top corner nodes given by  $\{x = L_x + \Delta L_x, y = L_y + \Delta L_y\}$  and  $\{x = -(L_x + \Delta L_x), y = L_y + \Delta L_y\}$  to locally model the ABCs.

In order to further suppress the spurious numerical reflections during the 2-D forward simulations, the incoming fluxes near the exterior computational boundary are damped over several nodes of a sponge-layer domain (6). The damping is implemented by multiplying the incoming fluxes with a Gaussian function which is unity at the nodes of the interior computational boundary and smoothly decays to zero at the nodes of the exterior computational boundary. The condition  $(\partial \tilde{v} / \partial x) \big|_{x = -L_x - \Delta L_x} = 0$  is also implemented to suppress the incoming waves at  $x = -L_x - \Delta L_x$  boundary that are advected by the mean flow, thereby preventing instability. It is noted that implementation of ABC (with or without the inclusion of sponge-layer domain) at the left, right and top exterior boundaries of the 2-D computational domain is crucial for the temporal stability of forward simulation of a pulse propagating in a free-space over a large time duration. The rigid wall condition is implemented by setting the normal velocity to zero, i.e.,

$$\tilde{v}(-L_x - \Delta L_x \leq x \leq L_x + \Delta L_x, y = -L_y) = 0, \quad (8)$$

at all nodes of the bottom ( $y = -L_y$ ) boundary after every time-step of integration and also by setting (24)

$$Y_{\text{linear}}^+(-L_x - \Delta L_x \leq x \leq L_x + \Delta L_x, y = -L_y) = Y_{\text{linear}}^-(-L_x - \Delta L_x \leq x \leq L_x + \Delta L_x, y = -L_y), \quad (9)$$

during every step of computing the acoustic fluxes. The forward simulations were carried out for a large time-interval  $t = [0, T = 10000\Delta t]$  during which the pulse completely propagates out of the 2-D domain.

## 2.2 TR Simulations

The acoustic pressure was stored at nodes of all four boundaries of computational domain, i.e. at  $x = \pm L_x$ , (the right and left boundaries, respectively) and at  $y = \pm L_y$ , (the top and bottom boundaries, respectively) during every time-step of forward simulation. The stored acoustic pressure time-history were

used as Dirichlet conditions at the boundary nodes during every TR time-step which enables back-propagation of waves into the computational domain (3). The 2-D LEE (in the PCF) for implementing the TR simulation is obtained by means of the following transformations (3, 5, 6, 16, 17) in Eqs. (2a-c)

$$t \rightarrow T - \tilde{t}, \quad \tilde{p}(x, y, t) \rightarrow \tilde{p}(x, y, \tilde{t}), \quad \tilde{u}(x, y, t) \rightarrow -\tilde{u}(x, y, \tilde{t}), \quad \tilde{v}(x, y, t) \rightarrow -\tilde{v}(x, y, \tilde{t}) \quad (10a-d)$$

to obtain the following set of time-reversed 2-D LEE.

$$\begin{aligned} \frac{\partial \tilde{p}}{\partial \tilde{t}} &= -\frac{\rho_0 c_0}{2} \left\{ (\tilde{X}_{\text{linear}}^+ + \tilde{X}_{\text{linear}}^-) + (\tilde{Y}_{\text{linear}}^+ + \tilde{Y}_{\text{linear}}^-) \right\}, \\ \frac{\partial \tilde{u}}{\partial \tilde{t}} &= -\frac{1}{2} (\tilde{X}_{\text{linear}}^+ - \tilde{X}_{\text{linear}}^-), \quad \frac{\partial \tilde{v}}{\partial \tilde{t}} = -\frac{1}{2} (\tilde{Y}_{\text{linear}}^+ - \tilde{Y}_{\text{linear}}^-) - c_0 (-M_0) \frac{\partial \tilde{v}}{\partial x}, \end{aligned} \quad (11a-c)$$

$$\text{where} \quad \tilde{X}_{\text{linear}}^\pm = \pm c_0 (1 \mp M_0) \left\{ \frac{1}{\rho_0 c_0} \frac{\partial \tilde{p}}{\partial x} \pm \frac{\partial \tilde{u}}{\partial x} \right\}, \quad \tilde{Y}_{\text{linear}}^\pm = \pm c_0 \left\{ \frac{1}{\rho_0 c_0} \frac{\partial \tilde{p}}{\partial y} \pm \frac{\partial \tilde{v}}{\partial y} \right\}, \quad (12a-d)$$

and  $\tilde{t}$  denotes the reverse time. It is noted that the time-reversed 2-D LEE given by Eqs. (12a-c) are identical to Eqs. (2a-c), except that the direction of subsonic mean flow is reversed in  $\tilde{X}_{\text{linear}}^\pm$  fluxes and in the  $(\partial \tilde{v} / \partial x)$  term. The reversal of mean flow direction ( $M_0 \rightarrow -M_0$ ) during the TR simulation (and not in the physical sense) is essential to ensure TR invariance (3, 6). Furthermore, the derivative  $(\partial \tilde{v} / \partial x)$  in Eq. (14c) is computed using Eq. (6) due to reversal of mean flow direction.

A parametric study was carried out to investigate the effect of a reflective surface on TR simulations using complete/partial boundary data, i.e., time-reversed acoustic pressure history. These numerical TR experiments comprises of TR simulations by enforcing time-reversed acoustic pressure history at nodes on either (1) all four computational boundaries, (2) the top, left and right boundaries, (3) top and bottom boundaries and (4) only at the top boundary in the first, second, third and fourth test-case, respectively. It is noted that the rigid wall condition given by Eqs. (8) and (9) were implemented during TR simulation to take into account, reflection of the back-propagated waves at  $y = -L_y$  boundary. In fact, the implementation of rigid wall condition was necessary for the stability of TR simulation. Furthermore, the ABCs were implemented at the left, right and the top boundaries during TR simulation by using the first-order CEM ABCs (22) and corner conditions (23). The incoming normal fluxes were set to zero, i.e.,

$$\tilde{X}_{\text{linear}}^+ (x = -L_x) = \tilde{X}_{\text{linear}}^- (x = L_x) = \tilde{Y}_{\text{linear}}^- (y = L_y) = 0 \quad \text{to reinforce the ABCs. The boundary condition}$$

$$\left( \frac{\partial \tilde{v}}{\partial x} \right)_{x=L_x} = 0 \quad \text{is implemented to suppress the incoming disturbances advected by the mean flow.}$$

### 3. SIMULATION RESULTS AND DISCUSSION

The initial acoustic pressure field is given by  $\tilde{p}(x, y, t=0) = \varepsilon e^{-\alpha \{(x-x_0)^2 + (y-y_0)^2\}}$ , a 2-D Gaussian function, where  $\alpha = 100 \text{ m}^{-2}$ ,  $\varepsilon = 0.1 \text{ Pa}$  (a steep pulse of a small magnitude) and  $x_0 = 0$ ,  $y_0 = -0.25 \text{ m}$  denotes the specified initial location (near the wall) in the 2-D domain  $|x| \leq 1.65 \text{ m}$ ,  $-0.5 \text{ m} \leq y \leq 0.65 \text{ m}$ .

#### 3.1 Forward Simulation

Figures 2(a-f) depict the spatio-temporal evolution of the Gaussian pulse in the 2-D semi-infinite free-space over the computational domain  $|x| \leq 1.65 \text{ m}$ ,  $-0.5 \text{ m} \leq y \leq 0.65 \text{ m}$  obtained by the forward simulation at time-instants given by (a)  $t=0$  (Initial condition), (b)  $t=150\Delta t$ , (c)  $t=300\Delta t$ ,

(d)  $t = 500\Delta t$ , (e)  $t = 1000\Delta t$  and (f)  $t = 1500\Delta t$ , respectively. It is noted that the domain shown in Figs. 2(a-f) includes the sponge-layer domain necessary to damp the incoming spurious reflections at the exterior computational boundaries. In Figs. 2(a-f), the direction of the uniform mean flow along the positive  $x$  direction is indicated by an arrow, the colorbar depicts the magnitude of acoustic pressure in  $\text{Pa}(\text{N}\cdot\text{m}^{-2})$  and the known location of the peak of the Gaussian pulse in Fig. 2(a) is indicated by a circle  $\mathbf{O}$ . (It is noted that different colorbar scales are used in Figs. 2(a-f).) The same symbol and unit conventions are also followed for the remaining 2-D simulations.

It is observed from Fig. 2(b) that at  $t = 150\Delta t$ , the Gaussian pulse expands equally in all directions and the wave front propagating towards the rigid wall is about to undergo reflection. It is noted that during the spatio-temporal expansion of the pulse, its centre is convected towards the positive  $x$  direction due to the mean flow. At  $t = 300\Delta t$ , the wave front propagating towards the wall is reflected off it whilst the wave front propagating towards the top boundary expands further. The acoustic pressure field at  $t = 500\Delta t$  shown in Fig. 2(d) depicts the formation of two distinct wave fronts, the wave front formed due to wall reflection expands and begins to propagate towards the top boundary but lags behind the other wave front. Figures 2(e) and (f) illustrate the gradual spatial expansion of these two distinct wave fronts and their eventual propagation outside the computational domain with further progress of forward simulation whereby the acoustic pressure time-history is recorded at all nodes on the four boundaries.

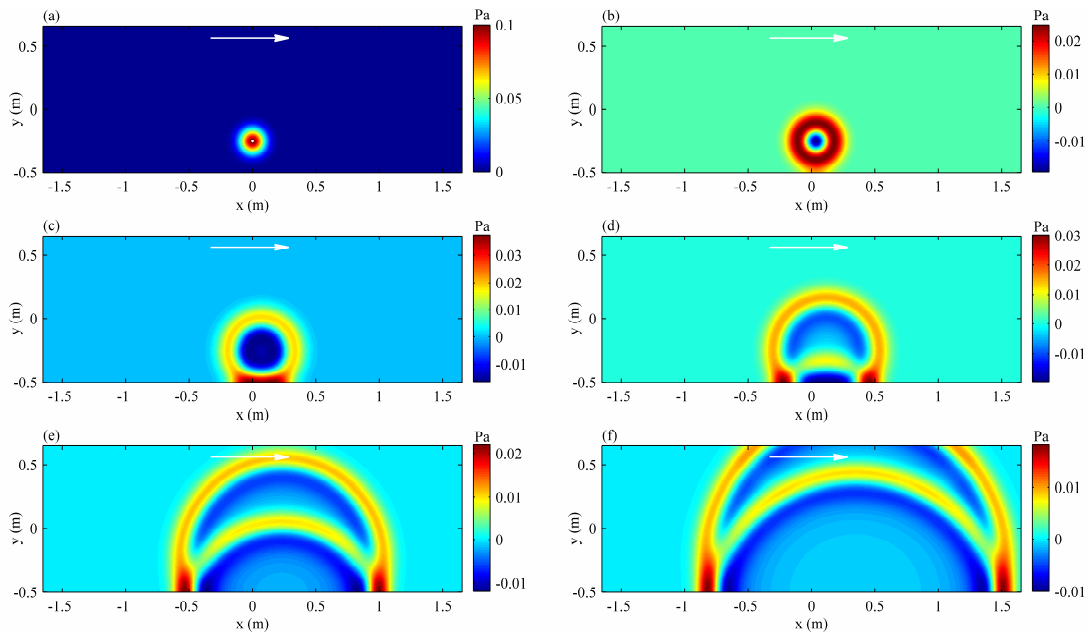


Figure 2 – Forward simulation of the acoustic pressure field  $\tilde{p}(x, y, t)$  depicting the spatio-temporal evolution of a Gaussian pulse in rectangular computational domain with a rigid wall at the bottom boundary and a uniform mean flow  $M_0 = 0.3$  towards the positive  $x$  direction at time-instants (a)  $t = 0$  (b)  $t = 150\Delta t$ , (c)  $t = 300\Delta t$ , (d)  $t = 500\Delta t$ , (e)  $t = 1000\Delta t$  and (f)  $t = 1500\Delta t$ .

### 3.2 TR Simulation: Back-propagation using complete or partial boundary data

Figures 3, 4, 5 and 6 depict the back-propagation or the time-reverse spatio-temporal evolution of the Gaussian pulse in the 2-D computational domain  $|x| \leq 1.5 \text{ m}$ ,  $|y| \leq 0.5 \text{ m}$  obtained by TR simulation using time-reversed acoustic pressure history at nodes (1) on all four boundaries, (2) on left, right and top boundaries, (3) on top and bottom boundaries and (4) on only the top boundary, respectively. In each of the Figs. 3 to 6, direction of the reversed uniform mean flow is indicated by an arrow. The parts (a-f) in Figs. 3 to 6 correspond to reverse time-instants given by (a)  $\tilde{t} = 8500\Delta t$ , (b)  $\tilde{t} = 9000\Delta t$ , (c)  $\tilde{t} = 9500\Delta t$ , (d)  $\tilde{t} = 9700\Delta t$ , (e)  $\tilde{t} = 9850\Delta t$  and (f)  $\tilde{t} = 10000\Delta t$ , respectively. It is noted that reverse time-instants  $\tilde{t} = [8500\Delta t, 9000\Delta t, 9500\Delta t, 9700\Delta t, 9850\Delta t, 10000\Delta t]$  correspond to the time-instants  $t = [0, 150\Delta t, 300\Delta t, 500\Delta t, 1000\Delta t, 1500\Delta t]$ , respectively, during forward simulation.

The TR acoustic pressure fields obtained in Figs. 3(a-f) are found to be identical with the acoustic pressure field shown in Figs. 2(f-a), respectively, obtained during forward simulation. In particular, Figs. 3(f) and 7 demonstrates that predicted location of the peak of the Gaussian pulse is coincident with the know location ( $x_0 = 0, y_0 = -0.25$  m) indicated in Fig. 2(a) and the strength of the pulse is also accurately retrieved. As expected, these results confirm that a highly accurate back-propagation of acoustic waves (or one-to-one correspondence of the forward field with the TR field) is possible through TR simulation by enforcing time-reversed acoustic pressure history at nodes on the computational boundary completely enclosing the source.

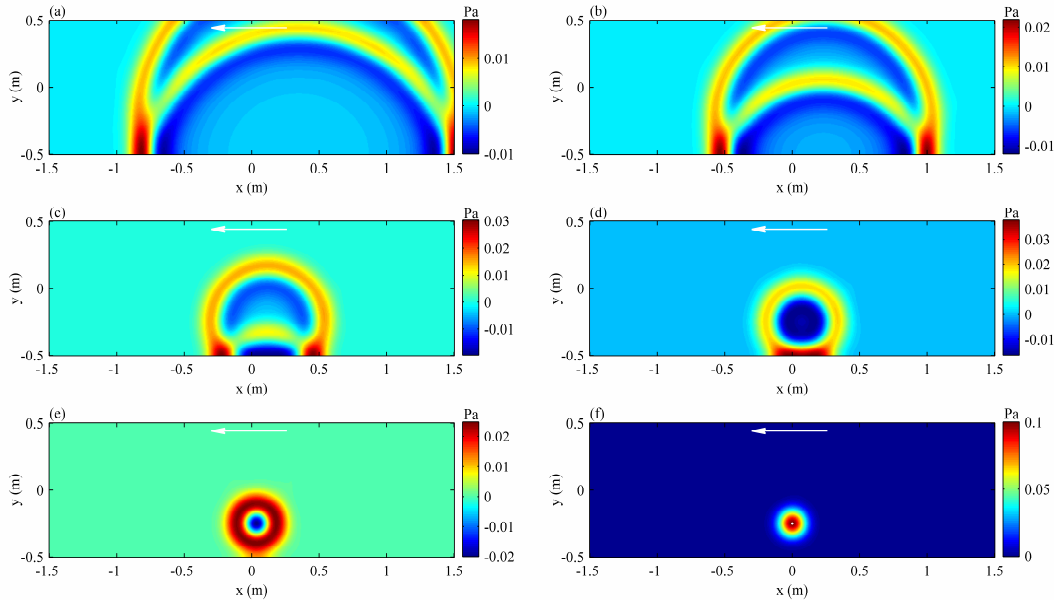


Figure 3 – TR simulation of the  $\tilde{p}(x, y, t)$  field depicting the back-propagation of Gaussian pulse in the 2-D domain using acoustic pressure time-history as input at nodes on all four boundaries.

A comparison of Figs. 4(a-f) with Figs. 2(f-a), respectively, indicate that these acoustic pressure fields are also identical. Indeed, Fig. 7 demonstrates an accurate localisation of the initial position of the peak of the Gaussian pulse as well as complete retrieval of strength of the pulse. This observation may be explained by means of the following discussion. In the presence of a rigid surface (bottom boundary), the acoustic waves propagating towards the wall are reflected, eventually propagate towards and are intercepted by the remaining three computational boundaries wherein the pressure history is stored at nodes (virtual microphones) at these boundaries. Therefore, despite not *directly* recording the acoustic pressure time-history at the bottom boundary, it is nonetheless possible to completely account for the acoustic waves that propagate towards this boundary by recording the time-history at the remaining three boundaries over larger time duration. This demonstrates that presence of rigid surface (owing to reflections) at a computational boundary compensates for the absence of recorded acoustic pressure time-history data and renders its use redundant at that boundary, provided that the remaining non-reflective boundaries in conjunction with the rigid boundary completely encloses the source. This result can potentially be used to reduce the number of microphones LAs required during an aeroacoustics experiment to record acoustic pressure time-history data for subsequent use in TR simulation.

Figures 5(f) and 6(f) indicate that although the initial location of the peak of the Gaussian pulse is accurately predicted, the strength is not completely retrieved. In fact, the strength of the pulse predicted by using the time-reversed acoustic pressure at only the top boundary is the least as is also indicated in Fig. 7. Furthermore, Figs. 6(a-f) indicate that although enforcing the time-reversed acoustic pressure at only the top boundary (in the presence of a reflecting surface) during TR back-propagates a significant portion of the acoustic power into the domain (due to interception of wave fronts during direct expansion of the pulse and reflection of the wall), the time-reversed spatio-temporal evolution of the acoustic pressure field is not identical with the corresponding forward fields shown in Figs. 2(a-f), respectively. This discrepancy is also observed in Figs. 5(a-f) and is attributed to absence of enforced time-history data (or LAs) during TR at the left and right boundaries.

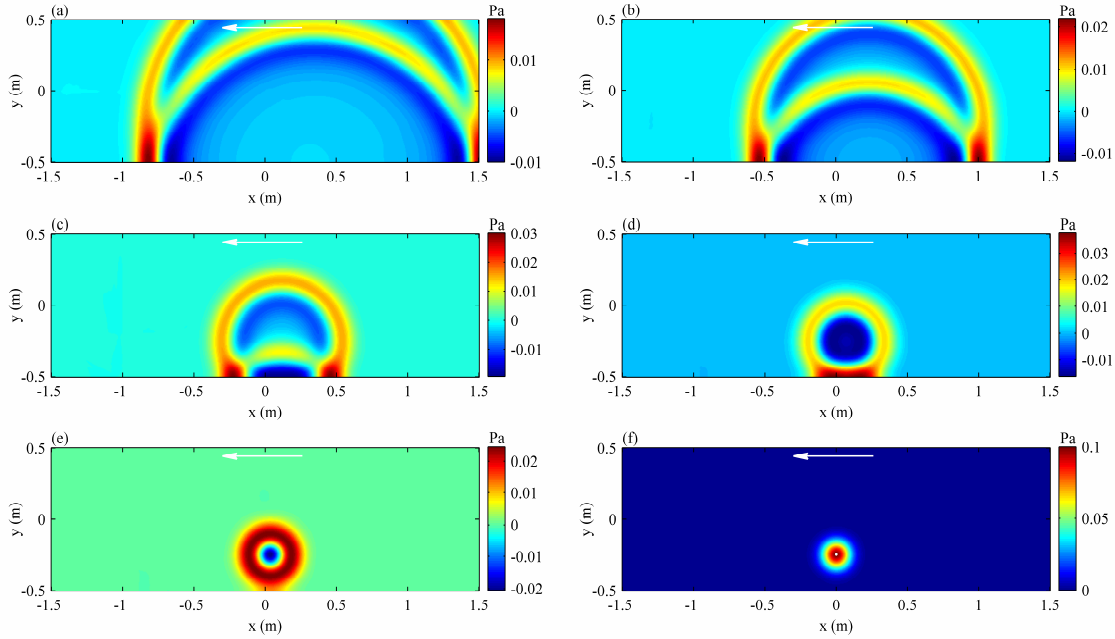


Figure 4 – TR simulation of the  $\tilde{p}(x, y, t)$  field depicting the back-propagation of Gaussian pulse in the 2-D domain using acoustic pressure time-history as input at nodes on the top, left and right boundaries.

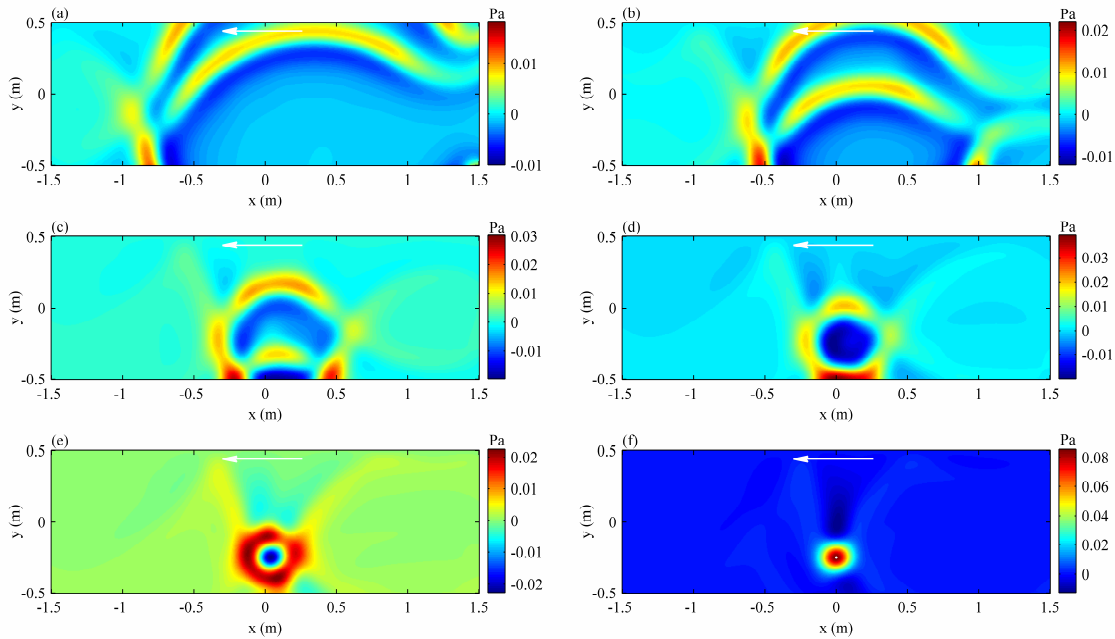


Figure 5 – TR simulation of the  $\tilde{p}(x, y, t)$  field depicting the back-propagation of Gaussian pulse in the 2-D domain using acoustic pressure time-history as input at nodes on the top and bottom boundaries.

The use of only top boundary data is equivalent to a limited effective angular aperture that can intercept/record only a partial amount of acoustic waves reflected by the wall, hence, resulting in a relatively small TR focusing. On other hand, use of both the top and bottom boundary data results in a somewhat increased effective angular aperture due to directly intercepting/recording of wave fronts propagating towards the wall, therefore, resulting in a better TR focusing. Indeed, numerical TR experiments (simulations) have revealed that for a low aspect-ratio  $L_y/L_x \approx 1$  of the computational domain, the strength of the pulse predicted by using both the top and bottom boundary data is twice that predicted by using only the top boundary data. In fact, as the  $L_y/L_x$  ratio increases, strength of the

pulse predicted by using both the top and bottom boundary data approaches the pulse strength predicted using only the top boundary data.

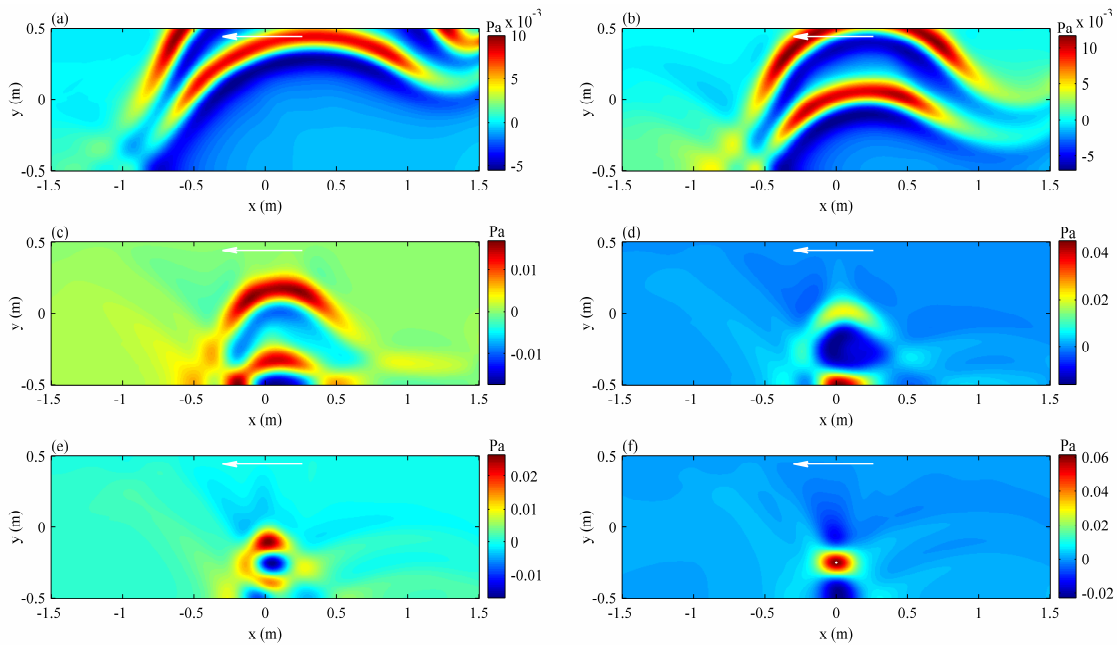


Figure 6 – TR simulation of the  $\tilde{p}(x, y, t)$  field depicting the back-propagation of Gaussian pulse in the 2-D domain using acoustic pressure time-history as input at nodes only on the top boundary.

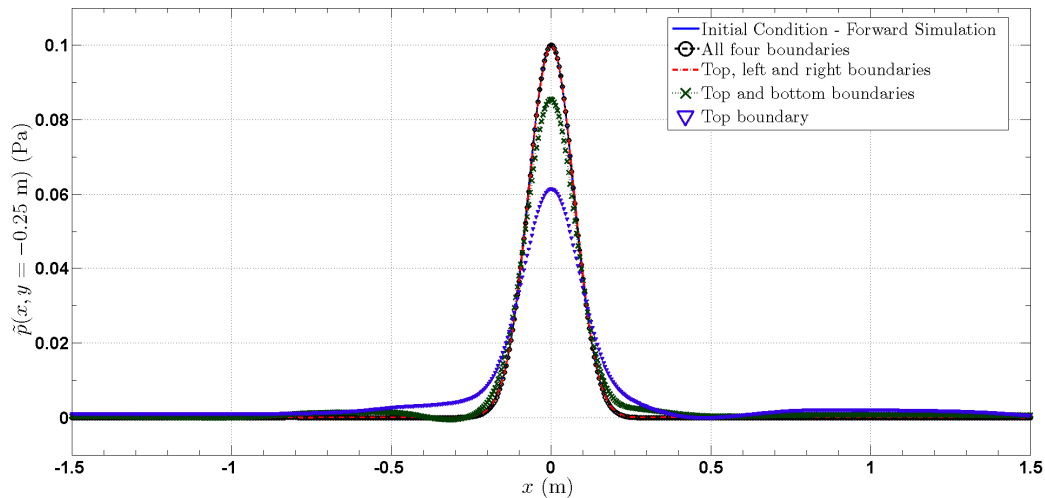


Figure 7 – Comparison of the acoustic pressure field along the  $x$  axis, i.e.,  $\tilde{p}(x, y = -0.25 \text{ m})$  obtained at the final time-instant  $\tilde{t} = 10000\Delta t$  during TR (Figs. 3(f), 4(f), 5(f) and 6(f)) with that at the beginning of forward simulation (initial condition).

#### 4. CONCLUSIONS

The influence of a rigid-wall reflecting surface on aeroacoustic Time-Reversal (TR) has been investigated through simulations of acoustic pulse propagation implemented using a high-resolution Computational AeroAcoustics (CAA) algorithm. It is shown that the wave fronts propagating towards a rigid boundary are reflected, subsequently intercepted and recorded at the remaining non-reflective boundaries. This can partially compensate for the absence of acoustic pressure history data at the rigid surface and potentially reduce the number of microphone LAs required during aeroacoustics experiment for TR source characterisation. For example, the floor of Anechoic Wind Tunnel (AWT) may be covered with a rigid surface (such as plywood to cause reflection), in such an experimental set-up, a single microphone LA (located at the top) can record sufficient acoustic pressure time-history

data for *characterising* a lift-dipole at the Aeolian tone generated due to cross-flow over a uniform cylinder which normally requires two LAs located at top and bottom boundaries of the AWT (25).

## ACKNOWLEDGEMENTS

The Australian Research Council is gratefully acknowledged for their support of this work through Discovery grant DP 120102134 'Resolving the mechanics of turbulent noise production'.

## REFERENCES

1. Fink M, Cassereau D, Derode A, Prada C, Roux P, Tanter M, Thomas JL, Wu F. Time-reversed acoustics, *Rep Prog Phys*. 2000; 63(12): 1933-1995.
2. Fink M, Prada C. Acoustical time-reversal mirrors, *Inverse Probl*. 2001; 17: R1-R38.
3. Padois T, Prax C, Valeau V, Marx D. Experimental localization of an acoustic source in a wind-tunnel flow by using a numerical time-reversal technique, *J Acoust Soc Am*. 2012; 132(4): 2397-2407.
4. Harker BM, Anderson BE. Optimization of the array mirror for time reversal techniques used in half-space environment, *J Acoust Soc Am*. 2013; 133: EL351-EL357.
5. Mimani A, Doolan CJ, Medwell PR. Multiple line arrays for the characterization of aeroacoustic sources using a time-reversal method, *J Acoust Soc Am*. 2013; 134: EL327-EL333.
6. Deneuve A, Druault P, Marchiano R, Sagaut P. A coupled time-reversal/complex differentiation method for aeroacoustic sensitivity analysis: towards a source detection procedure, *J Fluid Mech*. 2010; 642, 181-212.
7. Johnson DH, Dudgeon DE. *Array Signal Processing*, Englewood Cliffs, NJ, USA: Prentice Hall; 1993.
8. Blake WK, *Mechanics of Flow-Induced Sound and Vibration*, NY, USA: Academic Press; 1986.
9. Hillion P, Acoustic pulse reflection at a time-reversal mirror, *J Sound and Vib*. 2006; 292: 488-503.
10. Lerosey G, Rosny JD, Tourin A, Derode A, Montaldo G, Fink M. Time reversal of electromagnetic waves, *Phys. Rev. Lett*. 2004; 92: 193904.
11. Ribay G, Rosny J de, Fink M. Time reversal of noise sources in a reverberation room, *J Acoust Soc Am*. 2005; 117, 2866-2872.
12. Derode A, Tourin A, Fink M. Limits of time-reversal focusing through multiple scattering: Long-range correlation, *J Acoust Soc Am*. 2000; 107, 2987-2998.
13. Tam CKW, *Computational aeroacoustics: A wave number approach*, New York, USA: Cambridge University Press, 2012.
14. Bailly C, Juve D. Numerical solution of acoustic wave propagation problems using linearized Euler equations, *AIAA J*. 2000; 38, 22-29.
15. Sesterhenn J. A characteristic-type formulation of the Navier-Stokes equations for high order upwind schemes, *Comput. Fluids*. 2001; 30, 37-67.
16. Mimani A, Doolan CJ, Medwell PR. Stability and accuracy of aeroacoustic time-reversal using the pseudo-characteristic formulation, under Review in *Int J Acoust Vibr*.
17. Mimani A, Prime Z, Doolan CJ, Medwell PR. A sponge-layer damping technique for aeroacoustic time-reversal, under Review in *J Sound and Vib*.
18. Zhuang M, Chen RF. Applications of high-order optimized upwind schemes for computational aeroacoustics, *AIAA J*. 2002; 40, 443-449.
19. Li Y. Wavenumber-extended high-order upwind-biased finite-difference schemes for convective scalar transport, *J Comput Phys*. 1997; 133, 235-255.
20. Tam CKW, *Computational aeroacoustics: Issues and methods*, *AIAA J*. 1995; 33, 1788-1796.
21. Gottlieb S, Shu C-W. Total variation diminishing Runge-Kutta schemes, *Math Comput*. 1998; 67, 73-85.
22. Clayton R, Engquist, B. Absorbing boundary conditions for acoustic and elastic wave equations, *B Seismol Soc Am*. 1977; 67, 1529-1540.
23. Engquist B, Majda A. Radiation boundary conditions for acoustic and elastic wave calculations, *Commun Pur Appl Math*, 1979; 32, 313-357.
24. Lu S-Yi, Sagaut, P. Pseudo-characteristic formulation and dynamic boundary conditions for computational aeroacoustics, *Int J Numer Methods Fluids*, 2007; 53, 201-227.
25. Prime Z, Mimani A, Moreau DJ, Doolan CJ. An experimental comparison of beamforming, time-reversal and near-field acoustic holography for aeroacoustic source localization, *Proc 20<sup>th</sup> AIAA/CEAS Aeroacoustics Conference*, 16-20 June 2014; Atlanta, Georgia, USA 2014. Paper No. 2917.